Short Paper

Intrinsic Wrench Estimation and Its Performance Index for Multisegment Continuum Robots

Kai Xu and Nabil Simaan

***Abstract*—This paper presents the intrinsic capability of full-wrench estimation of multisegment continuum robots with multiple flexible backbones. Intrinsic-full-wrench estimation refers to the ability of continuum robots to also serve as force and moment sensors by using measurements of axial loads on their backbones. This end-effector-as-sensor approach fulfills the rapidly increasing needs for miniature-robotic-surgical tools with haptic sensing ability subject to various limitations, such as size, magnetic resonance imaging (MRI) compatibility, sterilizability, etc. A performance index for the intrinsic wrench-sensing capability is introduced and evaluated to show how this index can serve as a design guide for continuum robots that provide force sensing.**

***Index Terms*—Continuum robots, force sensing, haptic feedback, performance index, surgical assistant.**

I. Introduction

In robot-assisted surgery, force feedback has been shown to be an important factor for improved patient safety, precise manipulation, grasping or palpation of soft organs, and for improved transparency in master/slave teleoperation [1]–[5]. Hence, recent works have focused on providing surgical tools with force-sensing capabilities [6]–[10] by designing miniature force sensors to be placed at the distal end of surgical devices or by using joint-level information to quantify the applied forces.

Placing a dedicated multiaxis force sensor at the tip of surgical end-effectors offers a direct measurement of the interaction forces. However, increasing demands for magnetic resonance imaging (MRI) compatibility, sterilizability, and miniaturization of surgical end-effectors limit this approach. This paper answers the need for down-scalable surgical devices with force-sensing capability but with no end-effector force sensors. This type of wrench sensing using joint-level information is hereby referred to as *intrinsic wrench sensing*. According to this approach, the entire robot is used as a multiaxis force sensor by measuring active joint forces via load cells. This *end-effector-as-sensor* approach offers practical advantages such as reduced fabrication complexity, increased reliability, sterilizability, MRI compatibility, further miniaturization, etc.

Manuscript received April 22, 2009; revised December 16, 2009; accepted March 23, 2010. Date of publication May 6, 2010; date of current version June 9, 2010. This paper was recommended for publication by Associate Editor C. C. Cheah and Editor K. Lynch upon evaluation of the reviewers' comments. The work of K. Xu was supported in part by the National Science Foundation (NSF) under Engineering Research Center Grant EEC9731748, in part by the NSF Grant IIS9801684, and in part by Columbia University internal funds. The work of N. Simaan was supported in part by NSF CAREER Award 0844969.

K. Xu was with the Department of Mechanical Engineering, Columbia University, New York, NY 10027, USA. He is now with the University of Michigan-Shanghai Jiao Tong University Joint Institute, Shanghai Jiao Tong University, Shanghai 200240, China (e-mail: k.xu@sjtu.edu.cn).

N. Simaan is with the Department of Mechanical Engineering, Columbia University, New York, NY 10027 USA (e-mail: ns2236@columbia.edu).

Color versions of one or more of the figures in this paper are available online at http://ieeexplore.ieee.org.

Digital Object Identifier 10.1109/TRO.2010.2046924

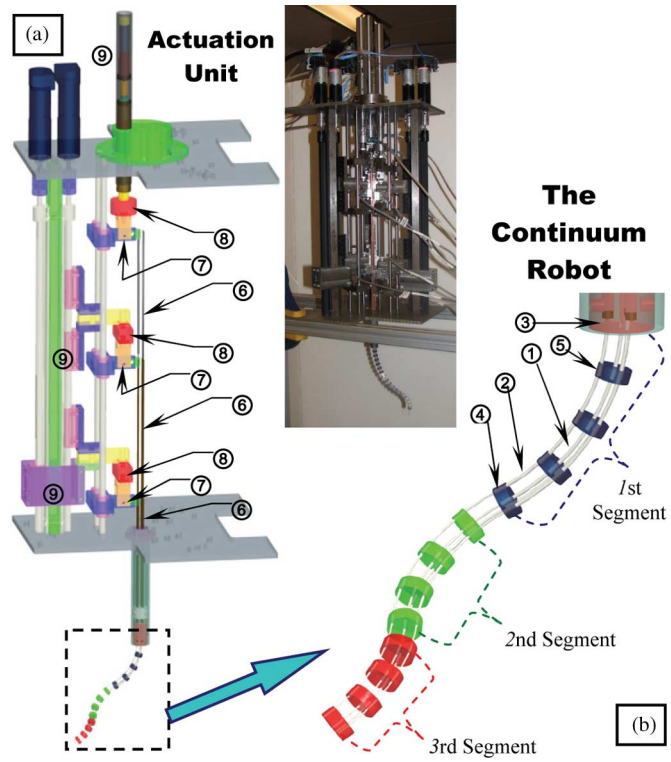

Fig. 1. A 7.5-mm continuum robot with three segments.

An attempt for this *end-effector-as-sensor* approach was presented in [11]. However, concerns about actual implementation were not answered until a preliminary study in [12] presented a new type of multibackbone continuum robots with the intrinsic-force-sensing capability. This force-sensing capability was attributed to a large magnification of the external forces when transformed into joint loads. A similar approach was presented in [13] using a nearly singular Stewart/Gough platform. The difference between the approaches given in [12] and [13], respectively, is that the force-magnification property in [12] is relatively consistent across the workspace—not just for poses near singularities.

Contribution: This paper extends the intrinsic-force-sensing algorithm for single-segment continuum robots, which is presented in [12], to full-wrench estimation for multisegment continuum robots. The paper also introduces a performance index for the intrinsic wrench-sensing capability. This index is derived and compared with a well-accepted evaluation index for load-cell designs as in [14]–[16]. This performance index is used for synthesis of continuum robots with intrinsic-force sensing.

II. Nomenclature and Kinematics Modeling

Both the actual structure and the computer-aided design (CAD) model of a 7.5-mm three-segment continuum robot and its actuation unit are shown in Fig. 1. Fig. 1(a) shows the actual experimental apparatus, while the CAD model shows only one third of the actuation unit for improved visualization. This design is inspired by the works of Hirose [17] and Gravagne and Walker [18], [19].

This continuum robot has three segments, which are numbered from the proximal to the distal end (where proximity is measured with respect

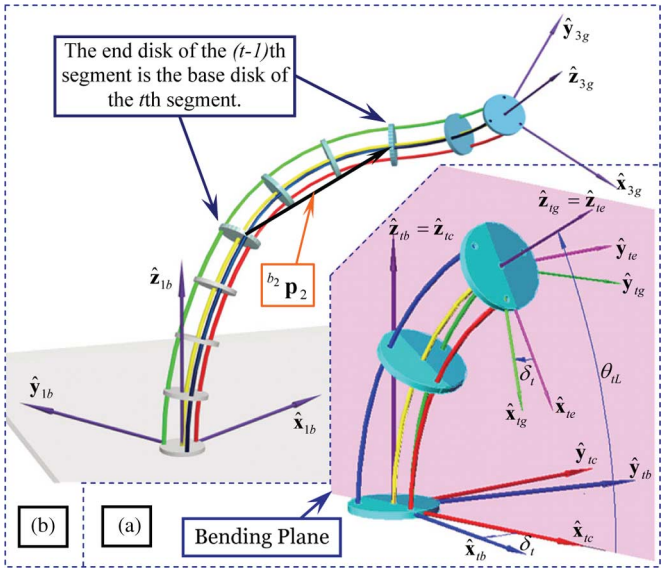

Fig. 2. Kinematics nomenclature for a three-segment continuum robot.

to the base). Each segment consists of four superelastic nickel–titanium (NiTi) alloy *backbones* and several disks. One *primary backbone* (see Fig. 1①) is centrally located, and three identical *secondary backbones* (see Fig. 1②) are equidistant from each other and from the primary backbone. For each segment, the primary backbone is attached to the base disk (see Fig. 1③) and the end disk (see Fig. 1④), while the secondary backbones are only attached to the end disk and can slide in appropriately toleranced holes in the base disk and in the spacer disks (see Fig. 1⑤), respectively. The end disk of the $(t\text{-}1)$th segment acts as the base disk of the tth segment. In order to minimize friction in the system, all the spacer disks are made from polytetrafluoroethylene (PTFE). Backbones of the first and second segment are concentric NiTi tubes, while the backbones of the third segment are NiTi beams, which pass through the backbone tubes of the second segment.

In Fig. 1, each secondary backbone of the three segments is driven in the push–pull mode by the concentric actuation tubes and rods (see Fig. 1⑥). Actuation cantilevers (see Fig. 1⑦) drive the actuation rods with load cells Omega-LC703 and Omega-LCFA (see Fig. 1⑧), which measure the actuation forces. The actuation cantilevers are supported on linear ball bearings and can slide freely along the actuation rails. Motorized lead screw actuators (see Fig. 1⑨) drive these actuation cantilevers. All the actuation components and load cells were designed to be sufficiently rigid to render their deformation negligible.

Each segment provides two degrees-of-freedom (DOF) bending motion through simultaneous actuation of its three secondary backbones, and 6-DOF motion is achieved by three serially connected segments.

A. Nomenclature

The three segments of the continuum robot are structurally similar. Fig. 2(a) shows one segment of the continuum robot, while Table I presents the nomenclature. The following coordinate systems are defined for the tth segment:

1) base disk coordinate system (BDS) $\{b_t\} \equiv \{\hat{\mathbf{x}}_{tb}, \hat{\mathbf{y}}_{tb}, \hat{\mathbf{z}}_{tb}\}$;
2) bending plane coordinate system (BPS) $\{c_t\} \equiv \{\hat{\mathbf{x}}_{tc}, \hat{\mathbf{y}}_{tc}, \hat{\mathbf{z}}_{tc}\}$;
3) end disk coordinate system (EDS) $\{e_t\} \equiv \{\hat{\mathbf{x}}_{te}, \hat{\mathbf{y}}_{te}, \hat{\mathbf{z}}_{te}\}$;
4) gripper coordinate system (GCS) $\{g_t\} \equiv \{\hat{\mathbf{x}}_{tg}, \hat{\mathbf{y}}_{tg}, \hat{\mathbf{z}}_{tg}\}$.

TABLE I
NOMENCLATURE USED IN THIS PAPER

t	Index of the segments, $t = 1,2,\ldots,n$. $n=3$ in Fig. 1.
${}^{b}x_t$	Entity x of the tth segment described in frame $\{b\}$. The left most subscript always designates the index of the segment.
x_t, x_{ti}	Entity x of the primary and the ith secondary backbone of the tth segment. Entity x can be s (arc length along a segment's primary backbone), L (length), E (Young's modulus), I (cross-sectional moments), D and d (outer and inner diameter).
$\mathbf{q}_t$	$\mathbf{q}_t = [q_{t1} \quad q_{t2} \quad q_{t3}]^T$ is the vector of the joint values of the tth segment, where $q_{ti} \equiv L_{ti} - L_t$.
$\mathbf{q}_{(n)}$	$\mathbf{q}_{(n)} = [\mathbf{q}_1^T \quad \mathbf{q}_2^T \quad \cdots \quad \mathbf{q}_n^T]^T$ is the augmented vector of joint values for an n-segment robot.
$\boldsymbol{\psi}_t$	$\boldsymbol{\psi}_t = [\theta_{tL} \quad \delta_t]^T$ is a configuration vector to define the pose of the tth segment of the robot.
$\boldsymbol{\psi}_{(n)}$	$\boldsymbol{\psi}_{(n)} = [\boldsymbol{\psi}_1^T \quad \boldsymbol{\psi}_2^T \quad \cdots \quad \boldsymbol{\psi}_n^T]^T$ is the augmented configuration vector that defines the pose of an n-segment continuum robot.
$\boldsymbol{\tau}_t$	$\boldsymbol{\tau}_t = [\tau_{t1} \quad \tau_{t2} \quad \tau_{t3}]^T$ is the vector of the joint forces of the tth segment.
$\boldsymbol{\tau}_{(n)}$	$\boldsymbol{\tau}_{(n)} = [\boldsymbol{\tau}_1^T \quad \boldsymbol{\tau}_2^T \quad \cdots \quad \boldsymbol{\tau}_n^T]^T$ is the augmented vector of the actuation forces for an n-segment continuum robot.
$\mathbf{J}_{t\mathbf{x}\boldsymbol{\psi}}$	$\dot{\mathbf{x}}_t = \mathbf{J}_{t\mathbf{x}\boldsymbol{\psi}}\dot{\boldsymbol{\psi}}_t$ where $\dot{\mathbf{x}}_t$ (the linear velocity precedes the angular velocity) is the twist of the end disk of the tth segment in $\{b_t\}$.
$\mathbf{J}_{t\mathbf{q}\boldsymbol{\psi}}$	Jacobian matrix of the mapping $\dot{\mathbf{q}}_t = \mathbf{J}_{t\mathbf{q}\boldsymbol{\psi}}\dot{\boldsymbol{\psi}}_t$
$\nabla\mathbf{E}_t$	Elastic energy gradient for the tth segment
$\mathbf{J}_{nx}$	Jacobian matrix for an n-segment continuum robot where $\dot{\mathbf{x}} = \mathbf{J}_{nx}\dot{\boldsymbol{\psi}}_{(n)}$, and $\dot{\mathbf{x}}$ is the twist of the end disk of the nth segment in $\{b_1\}$.
${}^{1}\mathbf{R}_2$	Rotation matrix of frame 2 with respect to frame 1.
${}^{b_k}\mathbf{p}_t(s_t)$	The relative position of a point along the primary backbone of the tth segment with respect to the tth base disk in $\{b_k\}$. The short notation ${}^{b_k}\mathbf{p}_t$ is used to designate ${}^{b_k}\mathbf{p}_t(L_t)$.
$\hat{\mathbf{g}}$	Vector for the gravitational acceleration
$\mathrm{c}_\alpha, \mathrm{s}_\alpha$	Shortened notation for $\cos\alpha$ and $\sin\alpha$

Notes: definitions of i, r, β, $\theta_t(s)$, θ_{tL}, δ_{ti}, and δ_t are identical to those entities in Table I of [12] with the same symbols except that a subscript t is added to represent different segments.

Definitions of $\{b_t\}$, $\{c_t\}$, $\{e_t\}$, and $\{g_t\}$ are identical to the definitions of the BDS, BPS, EDS, and GCS coordinates from [12], except that a subscript t is added to distinguish different segments.

B. Kinematics for One Segment

The kinematics of the single-segment continuum robots was addressed in [12] and [19]–[22], respectively, in which the bending shape of the continuum robot was assumed to be circular. For completeness, the kinematics are summarized here, based on [12] and [21], respectively.

For the tth segment of an n-segment continuum robot, the instantaneous direct kinematics from the configuration space to the twist space is then given by

$$\dot{\mathbf{x}}_t = \mathbf{J}_{t\mathbf{x}\boldsymbol{\psi}}\dot{\boldsymbol{\psi}}_t. \tag{1}$$

The inverse kinematics and the instantaneous inverse kinematics from the configuration space to the joint space are given, respectively, as the following:

$$L_{ti} = L_t + q_{ti} = L_t + r\cos(\delta_{ti})(\theta_{tL} - \theta_0), \quad i = 1,2,3 \tag{2}$$

$$\dot{\mathbf{q}}_t = \mathbf{J}_{t\mathbf{q}\boldsymbol{\psi}}\dot{\boldsymbol{\psi}}_t. \tag{3}$$

where the analytic expressions of $\mathbf{J}_{t\mathbf{x}\boldsymbol{\psi}}$ and $\mathbf{J}_{t\mathbf{q}\boldsymbol{\psi}}$ have been given by (6) and (9), respectively, in [12].

The rotation matrix ${}^{b_t}\mathbf{R}_{g_t}$, which associates different coordinate systems can be written as follows:

$$ {}^{b_t}\mathbf{R}_{g_t} = \mathrm{Rot}(\hat{\mathbf{z}}_{tb}, -\delta_t)\mathrm{Rot}(\hat{\mathbf{y}}_{tc}, \theta_0 - \theta_{tL})\mathrm{Rot}(\hat{\mathbf{z}}_{te}, \delta_t) \quad (4) $$

where $\mathrm{Rot}(\hat{\mathbf{n}}, \phi)$ designates rotation about $\hat{\mathbf{n}}$ by ϕ.

C. Kinematics for Stacked Segments

Figs. 1 and 2 show that segments can be stacked to form a robot with more degrees of freedom. If the numbering for secondary backbones is consistent for adjacent segments, $\{g_t\}$ is identical to $\{b_{t+1}\}$, e.g., ${}^{b_t}\mathbf{R}_{g_t} = {}^{b_t}\mathbf{R}_{b_{t+1}}$.

For an n-segment continuum robot, the configuration can be characterized by $\boldsymbol{\psi}_{(n)}$, and its kinematics can be obtained by deriving linear and angular velocities of the end disk using $\mathbf{J}_{t\mathbf{x}\boldsymbol{\psi}}$, $t = 1, 2, \ldots, n$. For $n = 2$ and $n = 3$, the Jacobian matrices are given by

$$ {}^{b_1}\dot{\mathbf{x}} = \mathbf{J}_{2x}\dot{\boldsymbol{\psi}}_{(2)} = \mathbf{J}_{2x}\left[\,\dot{\boldsymbol{\psi}}_1^T \quad \dot{\boldsymbol{\psi}}_2^T\,\right]^T \quad (5) $$

$$ \mathbf{J}_{2x} = \begin{bmatrix} \mathbf{J}_{1\mathbf{v}\boldsymbol{\psi}} - \left({}^{b_1}\mathbf{p}_2\right)^{\wedge}\mathbf{J}_{1\boldsymbol{\omega}\boldsymbol{\psi}} & {}^{b_1}\mathbf{R}_{b_2}\mathbf{J}_{2\mathbf{v}\boldsymbol{\psi}} \\ \mathbf{J}_{1\boldsymbol{\omega}\boldsymbol{\psi}} & {}^{b_1}\mathbf{R}_{b_2}\mathbf{J}_{2\boldsymbol{\omega}\boldsymbol{\psi}} \end{bmatrix} \quad (6) $$

where $\mathbf{J}_{t\mathbf{v}\boldsymbol{\psi}}$ and $\mathbf{J}_{t\boldsymbol{\omega}\boldsymbol{\psi}}$ are the translation and orientation Jacobian matrices given by the top and the bottom three rows of $\mathbf{J}_{t\mathbf{x}\boldsymbol{\psi}}$, ${}^{b_1}\mathbf{p}_2 = {}^{b_1}\mathbf{R}_{b_2}{}^{b_2}\mathbf{p}_2$, and $(\mathbf{p})^{\wedge}$ is the skew-symmetric matrix of a vector $\mathbf{p}$

$$ {}^{b_1}\dot{\mathbf{x}} = \mathbf{J}_{3x}\dot{\boldsymbol{\psi}}_{(3)} = \mathbf{J}_{3x}\left[\,\dot{\boldsymbol{\psi}}_1^T \quad \dot{\boldsymbol{\psi}}_2^T \quad \dot{\boldsymbol{\psi}}_3^T\,\right]^T \quad (7) $$

$$ \mathbf{J}_{3x} = \begin{bmatrix} \mathbf{T}_1 & {}^{b_1}\mathbf{R}_{b_2}\mathbf{T}_2 & {}^{b_1}\mathbf{R}_{b_3}\mathbf{J}_{3\mathbf{v}\boldsymbol{\psi}} \\ \mathbf{J}_{1\boldsymbol{\omega}\boldsymbol{\psi}} & {}^{b_1}\mathbf{R}_{b_2}\mathbf{J}_{2\boldsymbol{\omega}\boldsymbol{\psi}} & {}^{b_1}\mathbf{R}_{b_3}\mathbf{J}_{3\boldsymbol{\omega}\boldsymbol{\psi}} \end{bmatrix} \quad (8) $$

where $\mathbf{T}_1 = \mathbf{J}_{1\mathbf{v}\boldsymbol{\psi}} - \left({}^{b_1}\mathbf{p}_2 + {}^{b_1}\mathbf{p}_3\right)^{\wedge}\mathbf{J}_{1\boldsymbol{\omega}\boldsymbol{\psi}}$, $\mathbf{T}_2 = \mathbf{J}_{2\mathbf{v}\boldsymbol{\psi}} - \left({}^{b_2}\mathbf{p}_3\right)^{\wedge}\mathbf{J}_{2\boldsymbol{\omega}\boldsymbol{\psi}}$, ${}^{b_2}\mathbf{p}_3 = {}^{b_2}\mathbf{R}_{b_3}{}^{b_3}\mathbf{p}_3$, ${}^{b_1}\mathbf{R}_{b_3} = {}^{b_1}\mathbf{R}_{b_2}{}^{b_2}\mathbf{R}_{b_3}$, and ${}^{b_1}\mathbf{p}_3 = {}^{b_1}\mathbf{R}_{b_3}{}^{b_3}\mathbf{p}_3$, respectively.

The augmented vector of the joint rates $\dot{\mathbf{q}}_{(n)}$ is related to $\dot{\boldsymbol{\psi}}_{(n)}$ as follows:

$$ \dot{\mathbf{q}}_{(n)} = \mathbf{J}_{nq}\dot{\boldsymbol{\psi}}_{(n)}. \quad (9) $$

The actuation unit in Fig. 1 needs the actuators of the second and third segments to move synchronously with those of the first segment. Taking this coupling effect into consideration, and using $\mathbf{J}_{t\mathbf{q}\boldsymbol{\psi}}$, we get the following results in the coupled Jacobian $\mathbf{J}_{nq}$:

$$ \mathbf{J}_{nq} = \begin{bmatrix} \mathbf{J}_{1\mathbf{q}\boldsymbol{\psi}} & \mathbf{0}_{3\times 2} & \cdots & \mathbf{0}_{3\times 2} \\ \mathbf{J}_{1\mathbf{q}\boldsymbol{\psi}} & \mathbf{J}_{2\mathbf{q}\boldsymbol{\psi}} & \cdots & \mathbf{0}_{3\times 2} \\ \vdots & \vdots & \ddots & \vdots \\ \mathbf{J}_{1\mathbf{q}\boldsymbol{\psi}} & \mathbf{J}_{2\mathbf{q}\boldsymbol{\psi}} & \cdots & \mathbf{J}_{n\mathbf{q}\boldsymbol{\psi}} \end{bmatrix}. \quad (10) $$

III. Intrinsic Wrench Sensing and Performance Index

A. Statics

The static analysis is based on a virtual-work model. Twisting, extension of backbones, and friction are neglected by following the same assumptions as described in [12].

For an n-segment continuum robot, an external wrench $\mathbf{W}_e = [\,\mathbf{f}_e^T \;\; \mathbf{m}_e^T\,]^T$ acts on the end disk of the distal (the nth) segment, where $\mathbf{f}_e$ indicates the force, and $\mathbf{m}_e$ indicates the moment. This external wrench perturbs the robot posture (position and orientation, respectively) of the end disk by $\boldsymbol{\Delta}\mathbf{x}$. For this pose perturbation, there are corresponding infinitesimal changes in the lengths of the secondary backbones of all its segments $\boldsymbol{\Delta}\mathbf{q}_{(n)}$. The actuation forces on the secondary backbones of all the segments, which maintain the robot's static equilibrium are $\boldsymbol{\tau}_{(n)}$. The change in the robot's potential energy ΔE that corresponds to $\boldsymbol{\Delta}\mathbf{x}$ is given by

$$ \mathbf{W}_e^T\boldsymbol{\Delta}\mathbf{x} + \boldsymbol{\tau}_{(n)}^T\boldsymbol{\Delta}\mathbf{q}_{(n)} = \Delta E. \quad (11) $$

The virtual displacement $\boldsymbol{\Delta}\mathbf{x}$ is related to $\boldsymbol{\Delta}\boldsymbol{\psi}_{(n)}$ by $\boldsymbol{\Delta}\mathbf{x} = \mathbf{J}_{nx}\boldsymbol{\Delta}\boldsymbol{\psi}_{(n)}$, and $\mathbf{J}_{3x}$ is presented in (8). $\boldsymbol{\Delta}\mathbf{q}_{(n)}$ is related to $\boldsymbol{\Delta}\boldsymbol{\psi}_{(n)}$ by $\boldsymbol{\Delta}\mathbf{q}_{(n)} = \mathbf{J}_{nq}\boldsymbol{\Delta}\boldsymbol{\psi}_{(n)}$.

Then, the virtual work principle is rewritten as in (12). The equilibrium condition requires the terms associated with each independent DOF to vanish. The matrix form of this system of linear equations is given in (13), where $\nabla\mathbf{E}_{(n)}$ represents the gradient of the elastic energy with respect to the configuration perturbation $\boldsymbol{\Delta}\boldsymbol{\psi}_{(n)}$ of one n-segment continuum robot

$$ \mathbf{W}_e^T\mathbf{J}_{nx}\boldsymbol{\Delta}\boldsymbol{\psi}_{(n)} + \boldsymbol{\tau}_{(n)}^T\mathbf{J}_{nq}\boldsymbol{\Delta}\boldsymbol{\psi}_{(n)} = \nabla\mathbf{E}_{(n)}^T\boldsymbol{\Delta}\boldsymbol{\psi}_{(n)} \quad (12) $$

$$ \mathbf{J}_{nq}^T\boldsymbol{\tau}_{(n)} + \mathbf{J}_{nx}^T\mathbf{W}_e = \nabla\mathbf{E}_{(n)}. \quad (13) $$

The total potential energy $E_{(n)}$ of the n-segment continuum robot consists of the gravitational potential energy and the elastic potential energy generated, as in (14), shown at the bottom of the page, where one segment is approximated as a circular arc with its total mass being uniformly distributed along its primary backbone, and γ is the average mass per unit length.

The gradient vector $\nabla\mathbf{E}_{(n)}$ can be obtained by taking derivative of (14) with respect to $\boldsymbol{\psi}_{(n)}$. In the actual implemented condition, the value of $\nabla\mathbf{E}_{(n)}$ is obtained numerically.

B. Intrinsic Wrench Sensing

Equation (13) can be rewritten as

$$ \mathbf{J}_{nx}^T\mathbf{W}_e = \nabla\mathbf{E}_{(n)} - \mathbf{J}_{nq}^T\boldsymbol{\tau}_{(n)}. \quad (15) $$

It is possible for the continuum robot to sense the wrench $\mathbf{W}_e$, if the actuation forces $\boldsymbol{\tau}_{(n)}$ are monitored by the load cells.

There are six unknown components in the external wrench $\mathbf{W}_e$. When $\mathbf{J}_{nx}^T$ is rank deficient, the general solutions of (15) for the sensed-wrench $\mathbf{W}_s$ can be written as follows:

$$ \mathbf{W}_s = \left(\mathbf{J}_{nx}^T\right)^{+}\left(\nabla\mathbf{E}_{(n)} - \mathbf{J}_{nq}^T\boldsymbol{\tau}_{(n)}\right) + \mathbf{N}\boldsymbol{\eta} \quad (16) $$

$$ E_{(n)} = \sum_{t=1}^{n}\left(\begin{array}{l} \displaystyle\int_0^{L_t}\frac{E_tI_t}{2}\left(\frac{d\theta_t}{ds}\right)^2 ds + \sum_{i=1}^{3}\left(\int_0^{L_{ti}}\frac{E_{ti}I_{ti}}{2}\left(\frac{d\theta_t}{ds}\right)^2 ds\right) \\ \qquad\qquad - \displaystyle\int_0^{L_t}\gamma\left[\sum_{j=1}^{t-1}\left({}^{b_1}\mathbf{p}_j\right) + {}^{b_1}\mathbf{p}_t\,(s)\right]^T {}^{b_1}\hat{\mathbf{g}}\,ds \end{array}\right) \quad (14) $$

where $(\mathbf{J}_{nx}^T)^+ = \mathbf{J}_{nx}(\mathbf{J}_{nx}^T\mathbf{J}_{nx})^{-1}$, and $\mathbf{N} = \mathbf{I} - (\mathbf{J}_{nx}^T)^+(\mathbf{J}_{nx}^T)$ is the null-space projector of $\mathbf{J}_{nx}^T$. The resolution for $\mathbf{W}_s$ in (16) depends on the joint-level information and also on an *a priori* knowledge as shown in [12] for a one-segment continuum robot.

When $\mathbf{J}_{nx}^T$ is full rank, the general solution of (15) is

$$\mathbf{W}_s = \left(\mathbf{J}_{nx}^T\right)^+ \left(\nabla\mathbf{E}_{(n)} - \mathbf{J}_{nq}^T\boldsymbol{\tau}_{(n)}\right) \tag{17}$$

where $(\mathbf{J}_{nx}^T)^+$ equals $(\mathbf{J}_{nx}^T)^{-1}$ if $\mathbf{J}_{nx}^T$ is square; otherwise, $(\mathbf{J}_{nx}^T)^+ = (\mathbf{J}_{nx}\mathbf{J}_{nx}^T)^{-1}\mathbf{J}_{nx}$.

C. Performance Index

Not all kinds of robots are suitable for the approach to utilize the intrinsic wrench sensing. A performance index is needed to evaluate different robots for the intrinsic wrench-sensing capabilities. In order to formulate the performance index, an error analysis is first conducted for the sensing model from (17) as follows:

$$\mathbf{W}_s = \mathbf{A}(\nabla\mathbf{E}_{(n)} - \mathbf{B}\boldsymbol{\tau}_{(n)}) \tag{18}$$

$$\mathbf{W}_s + \delta\mathbf{W}_s = (\mathbf{A}+\delta\mathbf{A})(\nabla\mathbf{E}_{(n)} + \delta\nabla\mathbf{E}_{(n)} - (\mathbf{B}+\delta\mathbf{B})(\boldsymbol{\tau}_{(n)} + \delta\boldsymbol{\tau}_{(n)})) \tag{19}$$

where $\mathbf{A} = (\mathbf{J}_{nx}^T)^+$, $\mathbf{B} = \mathbf{J}_{nq}^T$, and $\delta\mathbf{W}_s$ is the wrench-estimation error, $\delta\mathbf{A}$, $\delta\mathbf{B}$, and $\delta\nabla\mathbf{E}_{(n)}$ are system-modeling errors, and $\delta\boldsymbol{\tau}_{(n)}$ are measurement errors from robot's joints.

Equation (20) can be derived by expanding the terms of the right-hand side in (19), substituting (18), and neglecting the higher order perturbations ($\delta\mathbf{A}\delta\nabla\mathbf{E}_{(n)}$, $\delta\mathbf{A}\delta\mathbf{B}\delta\tau_{(n)}$, $\delta\mathbf{A}\mathbf{B}\delta\boldsymbol{\tau}_{(n)}$, $\mathbf{A}\delta\mathbf{B}\delta\boldsymbol{\tau}_{(n)}$, and $\delta\mathbf{A}\delta\mathbf{B}\delta\boldsymbol{\tau}_{(n)}$)

$$\delta\mathbf{W}_s = \delta\mathbf{A}\nabla\mathbf{E}_{(n)} + \mathbf{A}\delta\nabla\mathbf{E}_{(n)} - \delta\mathbf{A}\mathbf{B}\tau_{(n)} - \mathbf{A}\delta\mathbf{B}\tau_{(n)} - \mathbf{A}\mathbf{B}\delta\boldsymbol{\tau}_{(n)} \tag{20}$$

where $\delta\mathbf{W}_s$ in (20) has both force components and moment components, respectively. A projection matrix $\boldsymbol{\Lambda}$ can be used to normalize $\delta\mathbf{W}_s$

$$\boldsymbol{\Lambda}\delta\mathbf{W}_s = \boldsymbol{\Lambda}(\delta\mathbf{A}\nabla\mathbf{E}_{(n)} + \mathbf{A}\delta\nabla\mathbf{E}_{(n)} - \delta\mathbf{A}\mathbf{B}\boldsymbol{\tau}_{(n)} - \mathbf{A}\delta\mathbf{B}\boldsymbol{\tau}_{(n)} - \mathbf{A}\mathbf{B}\delta\boldsymbol{\tau}_{(n)}). \tag{21}$$

Here, $\boldsymbol{\Lambda}$ is assumed to be $\mathbf{I}_{6\times6}$, since normalizing $\delta\mathbf{W}_s$ with a unit length does not affect the generality of the analysis. When the proposed theory is applied to a specific robot design or evaluation, normalizing $\delta\mathbf{W}_s$ with a specific characteristic length can be considered.

To quantify the magnitude of this wrench-sensing error, the norm of $\delta\mathbf{W}_s$ needs to be examined. From (20) and according to [23], the magnitude of the wrench-estimation error $\|\delta\mathbf{W}_s\|$ can be shown to have an upper bound as in (22)

$$\|\delta\mathbf{W}_s\|_F = \|\delta\mathbf{W}_s\|_2 \le \|\delta\mathbf{A}\|_F\|\nabla\mathbf{E}_{(n)}\|_F + \|\mathbf{A}\|_F\|\delta\nabla\mathbf{E}_{(n)}\|_F + \|\delta\mathbf{A}\mathbf{B}\|_F\|\boldsymbol{\tau}_{(n)}\|_F + \|\mathbf{A}\delta\mathbf{B}\|_F\|\boldsymbol{\tau}_{(n)}\|_F + \|\mathbf{A}\mathbf{B}\|_F\|\delta\boldsymbol{\tau}_{(n)}\|_F \tag{22}$$

where $\|\|_2$ is the induced two-norm (Euclidian norm), and $\|\|_F$ is the Frobenius norm.

There are five terms, which contribute to the upper bound of the magnitude of the sensing errors. The first four terms depend largely on $\|\delta\mathbf{A}\|$, $\|\mathbf{A}\delta\mathbf{B}\|$, $\|\delta\mathbf{A}\mathbf{B}\|$, and $\|\delta\nabla\mathbf{E}_{(n)}\|$, respectively, which are all from system-modeling errors; they can be effectively reduced by a careful system calibration as presented in Section IV.

When fundamental feasibility of intrinsic wrench sensing is studied, the critical term is $\|\mathbf{A}\mathbf{B}\|\|\delta\boldsymbol{\tau}_{(n)}\|$ since this term will determine how the joint-level transducer errors affect the sensing results. In actual practices, $\|\delta\boldsymbol{\tau}_{(n)}\|$ might not be effectively reduced by simply implementing more expensive load cells, since it will be largely effected by friction, backlash, preload, mechanical wear, signal noises, etc. For this reason, $\|\mathbf{A}\mathbf{B}\|_F$ is selected as the performance index for the robot's intrinsic wrench-sensing capability. This performance index χ quantifies an upper bound of the wrench-sensing errors as a result of joint transducer errors

$$\chi_{\text{Continuum}} = \|(\mathbf{J}_{nx}^T)^+\mathbf{J}_{nq}^T\|_F. \tag{23}$$

A robot has better wrench-sensing capability if the evaluated index is smaller.

Related studies in [14]–[16] propose the condition number of corresponding sensing matrices as the evaluation indices for multiaxis sensor designs. Although the presented sensing approach is essentially treating the entire robot as one force sensor, the approaches in [14]–[16] are not followed here, since the condition number of $(\mathbf{J}_{nx}^T)^+\mathbf{J}_{nq}^T$ does not reward the Frobenius norm, which is more important in bounding the sensing errors.

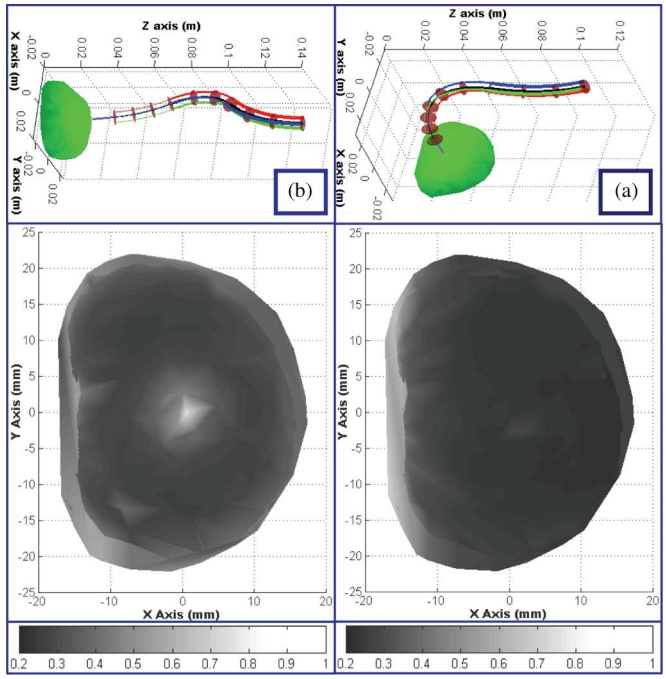

Fig. 3. Performance index for a three-segment continuum robot when it is palpating the prostate model. (a) Facing the facade and (b) from the side.

D. Simulation Case Study

In order to demonstrate the evaluation of the intrinsic wrench-sensing-performance index of a three-segment continuum robot in a realistic scenario, a simulation is conducted, where the robot palpates the upper surface of a digitized life-size prostate model. This prostate model ($50 \times 40 \times 16$ mm) was from GPI Anatomicals, Inc., Kennesaw, GA. The performance index is evaluated, when the attached probe touches the surface at predefined palpation points, while the palpation direction is the same as the surface normal at the palpation point.

Fig. 3 and multimedia extension I show the results of the simulation. In Fig. 3(a), the continuum robot is placed exactly above the prostate model. The performance index throughout the scanned surface varies from 0.23 to 0.76. In Fig. 3(b), the continuum robot approaches the prostate from the side, and the performance index varies from 0.21

TABLE II
PARAMETERS OF THE THREE-SEGMENT CONTINUUM ROBOT AS DESCRIBED IN FIG. 1

$r = 3.0mm$		$E_t = E_{ti} = 62GPa$
$L_1 = 50mm$	$D_1 = D_{1i} = 0.889mm$	$d_1 = d_{1i} = 0.762mm$
$L_2 = 40mm$	$D_2 = D_{2i} = 0.635mm$	$d_2 = d_{2i} = 0.508mm$
$L_3 = 30mm$	$D_3 = D_{3i} = 0.406mm$	$d_3 = d_{3i} = 0mm$
$\kappa_1 = 1.076$	$\kappa_2 = 1.075$	$\kappa_3 = 1.132$
$\theta_{1c} = 7.2°$	$\theta_{2c} = 7.3°$	$\theta_{3c} = 12.7°$

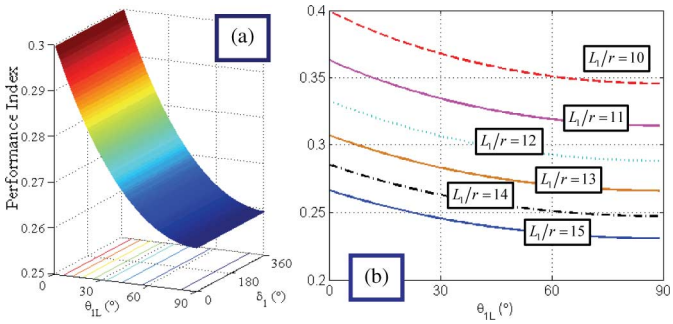

Fig. 4. Performance index (a) over configuration space for a one-segment robot (b) as design parameters vary.

to 0.73. Under both situations, an index value of 0.2 means that the errors from the joints measurements will be reduced five times when the external wrench is estimated. In other words, joint load cells with a resolution of 5 g can generate sensing results with a resolution of 1 g. The numerical values of the continuum robot can be found in Table II.

E. Robot Synthesis Using Performance Index

Performance index from (23) can also be applied in robot synthesis. For simplicity and with no loss of generality, a one-segment continuum robot will be considered.

To design a one-segment robot, there are two main parameters: L_1 and r. The performance index for a one-segment robot is presented in (24), shown below, and its evaluation over the configuration space is plotted in Fig. 4(a)

$$\chi_{\text{Continuum}} = \|(\mathbf{J}_{1x}^T)^+ \mathbf{J}_{1q}^T\|_F = \|(\mathbf{J}_{1\mathbf{x}\psi}^T)^+ \mathbf{J}_{1\mathbf{q}\psi}^T\|_F \qquad (24)$$

where $\mathbf{J}_{1\mathbf{x}\psi}$ and $\mathbf{J}_{1\mathbf{q}\psi}$ are from (6) and (9), respectively, in [12].

Results from Fig. 4(a) show that the performance index for a one-segment robot mainly depends on θ_{1L}. This can be intuitively explained by the fact that the performance index is fundamentally derived from formulation of the total potential energy (both gravitational and elastic, respectively). This total energy depends more on θ_{1L} value than on δ_1 value.

By virtue of the qualitative analysis reported in Fig. 4(a), the performance index is then evaluated for different L_1/r ratios as θ_{1L} varies. δ_1 is set zero since it does not affect the performance index significantly. r is a coefficient for $\mathbf{J}_{1\mathbf{q}\psi}$, and it is linearly proportional to the performance index value. This is another reason why the condition number is not selected as the performance index. Otherwise, the design parameter r would have no contribution to the performance evaluation at all.

From Fig. 4(b), L_1/r ratio is inversely proportional to the performance index. In other words, a slimmer robot will have better wrench-sensing capability. This figure can be used as a design chart for designers to quickly determine the initial design parameters. To obtain better wrench-sensing capability for a one-segment robot, a larger L_1/r value is preferred. However, the determination of the actual values should also take other considerations into account, such as workspace, strength limits of the backbones, stiffness, etc.

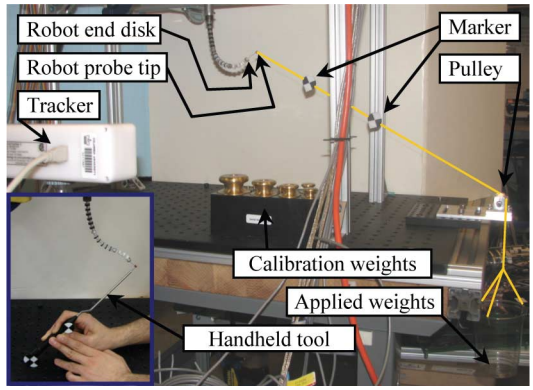

Fig. 5. Experimental setup for the intrinsic wrench sensing.

IV. EXPERIMENTAL CORRECTIONS FOR THE MODELING

The model presented in the previous sections assumes a perfectly circular-bending shape of each segment. In [12], this assumption was validated experimentally, and necessary correction factors that account for shape discrepancy between the ideal model and the actual shape of each segment were proposed. The correction factors were applied to correct the kinematics and the wrench-sensing models.

This experimental validation and correction process involves digitizing the shape of each segment using computer vision, as detailed in [12]. Results of the presented three-segment continuum robot are summarized as follows.

1) No correction is required on $\mathbf{J}_{t\mathbf{x}\psi}$.
2) $\mathbf{J}_{t\mathbf{q}\psi}$ needs to be corrected because the ideal shape of the secondary backbone is different from its actual shape under the push–pull actuation. Compensated L_{ti} values lead to corrected $\mathbf{J}_{t\mathbf{q}\psi}$ value from (26) and updated $\nabla\mathbf{E}_t$ value from (14) using (25)

$$L_{ti} = L_t + q_{ti} = L_t + r\cos(\delta_{ti})(\kappa_t\theta_{tL} - \theta_{tc}) \qquad (25)$$

$$\mathbf{J}_{t\mathbf{q}\psi} = r\begin{bmatrix} \kappa_t\cos(\delta_{t1}) & -(\kappa_t\theta_{tL} - \theta_{tc})\sin(\delta_{t1}) \\ \kappa_t\cos(\delta_{t2}) & -(\kappa_t\theta_{tL} - \theta_{tc})\sin(\delta_{t2}) \\ \kappa_t\cos(\delta_{t3}) & -(\kappa_t\theta_{tL} - \theta_{tc})\sin(\delta_{t3}) \end{bmatrix} \qquad (26)$$

where κ_t and θ_{tc} are both correction parameters for the tth segment of the robot. The numerical values of κ_t and θ_{tc} are listed in Table II.

V. EXPERIMENTAL VALIDATION

To validate the proposed wrench-sensing model, two experiments are set up. In the first experiment, calibration weights were used to quantify the sensing errors from the continuum robot. In the second experiment, the robot was used to detect the stiffness of a clinical-prostate model with realistic pathologic conditions.

A. Experiment I: Sense Wrenches Applied at the End Disk

Fig. 5 shows the first experimental setup. A Kevlar thread was attached to the tip of a 25-mm-long probe fixed to the end disk of the third segment of the robot. The Kevlar thread passed through a frictionless

TABLE III
EXPERIMENTAL RESULTS

$\theta_{1L}=60°, \delta_1=-45°, \theta_{2L}=30°, \delta_2=0°, \theta_{3L}=10°, \delta_3=150°$					
X-Y-Z components (grams)			X-Y-Z components (mNm)		
14.19	-0.61	4.51	0.2	-1.8	-0.8
14.08	0.1	4.87	0.2	-1.3	-0.3
23.62	-1.39	7.43	0.2	-2.6	-1.0
23.28	-1.93	8.23	0.2	-3.3	-1.2
33.11	-1.38	10.51	-0.9	-4.8	2.3
33.37	-0.40	10.94	0.25	-5.2	1.7
42.43	1.51	14.06	-0.6	-6.2	1.1
41.71	0.03	15.57	-6.3	-6.4	-0.5
$\theta_{1L}=50°, \delta_1=90°, \theta_{2L}=75°, \delta_2=30°, \theta_{3L}=10°, \delta_3=60°$					
X-Y-Z components (grams)			X-Y-Z components (mNm)		
13.55	5.65	4.55	1.4	-1.9	-1.8
13.71	5.30	4.90	0.4	-3.1	-3.2
22.64	9.53	7.31	2.5	-4.2	-2.1
23.03	9.36	7.67	1.9	-5.3	-3.5
31.73	13.14	10.35	3.9	-6.9	-3.2
31.75	12.95	10.54	5.5	-7.1	-4.8
40.83	16.89	13.18	5.0	-9.7	-3.0
40.68	16.84	13.34	6.5	-11.2	-4.8
$\theta_{1L}=60°, \delta_1=-150°, \theta_{2L}=60°, \delta_2=45°, \theta_{3L}=10°, \delta_3=60°$					
X-Y-Z components (grams)			X-Y-Z components (mNm)		
-13.40	0.31	6.56	1.1	2.2	2.2
-12.86	0.35	7.58	2.2	4.0	3.3
-21.99	0.40	11.64	1.7	4.2	3.0
-22.05	0.44	12.07	2.2	5.1	2.5
-30.68	-0.11	16.60	0.8	6.3	1.5
-29.17	-1.56	18.20	2.9	7.7	1.6
-39.14	0.21	21.85	0.6	8.2	1.1
-39.94	-0.38	25.42	2.6	9.7	1.9

pulley, which was mounted to an aluminum frame. Two markers (with each marker weighing 0.08 g) were aligned with the Kevlar thread to measure the direction of the applied force using an optical tracker. When the force is applied, the force magnitude equaled to the applied weight; the force direction was calculated from the positions of the two markers. The applied moment depended on the actual positions of the robot's end disk as well as the probe's tip. These two positions were read by pointing a handheld tool at these two points.

The robot was bent to different configurations. Under each configuration, known wrenches (forces and moments, respectively) were applied to the robot. The magnitude of applied forces varied from 15 to 45 g in increments of 10 g. The actuation forces on the secondary backbones were monitored using Omega LC703 and LCFA load cells coupled with a 12-bit A/D at $\pm$0.01-V measurement range. This experimental setup allowed a measurement resolution of $\pm$0.5 g. Since there may be some friction in the joints, the actual resolution is estimated to be about $\pm$10 g.

The wrench-sensing results are listed in Table III, where the actual values are in the gray-shaded cells, and the sensed components are in the white cells. Among the error values, for the force components, the average-sensing error was $-$0.35 g with a standard deviation of 0.94 g; for the moment components, the average-sensing error was 0.11 mN·m with a standard deviation of 1.70 mN·m. We note that there is an outlier in column 4 row 10. It might be due to an unlogged disturbance to the basket for the applied weights.

B. Experiment II: Detect Stiffness of Prostate Models

A life-size prostate model with a realistic pathological condition was registered with respect to the three-segment continuum robot using a handheld tool with the optical tracker, as shown in Fig. 6. This

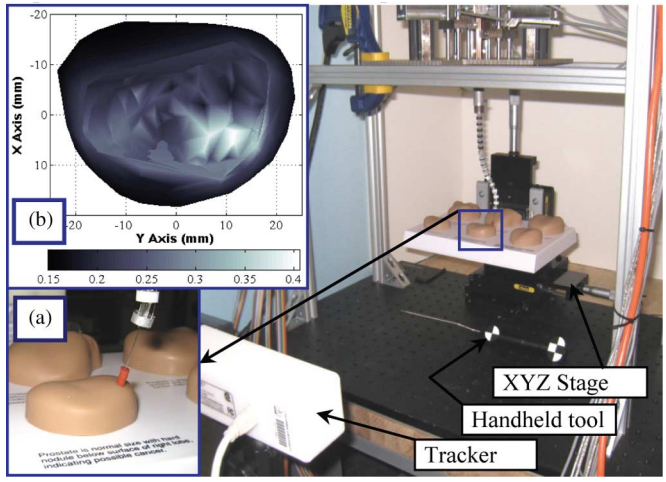

Fig. 6. Experimental setup for stiffness detection of prostate model. (a) Life-size prostate with hard nodule, which indicates the possibility of cancer. (b) Detected stiffness map of the prostate model.

prostate model is used for training physicians to detect pathological conditions by palpation. The prostate model used had a hard nodule below the surface of the right lobe, which indicates the possibility of cancer; see Fig. 6(a). The continuum robot probed the upper surface of the prostate model to detect the surface stiffness. The probing depth was 0.5 mm, and the surface was scanned by following the trajectory generated in the simulation presented in Section III-D. The stiffness value on a probed point was calculated as the ratio of resistance force over the probed depth. The resistance force was calculated using the wrench-sensing equation (17). Using the calculated stiffness value, the model of the prostate was reconstructed in Fig. 6(b). Two regions in the bottom-right portion of the model with higher surface stiffness were detected. These results agreed with the pathological condition mimicked by this prostate-training model. Multimedia extension II shows this experiment.

VI. CONCLUSION

Force sensing can help the surgical tools to improve safety in robot-assisted surgeries. An alternative approach of *intrinsic wrench sensing* was explored in this paper. According to this approach, axial loads on the backbones of a multisegment continuum robot were used to generate estimates of an unknown wrench acting at its tip. Thus, this *end-effector-as-sensor* approach fulfills the rapidly increasing needs for miniature tools with a force-sensing ability subject to various limitations, such as size, cost, MRI compatibility, and sterilizability.

A performance index that quantifies the quality of intrinsic wrench sensing for a given robot was presented. The importance of this performance index was demonstrated via a simulation case study for a three-segment continuum robot. A dimensional simulation showed that intrinsic force-sensing capability is improved by an increase in the slenderness of continuum robots. This simulation demonstrated the importance of this performance index as a design guide for continuum robots with improved intrinsic force-sensing capability.

Experimental validation of the efficacy of intrinsic force sensing was carried out on a three-segment continuum robot. The results showed that for a 6-D external wrench, the force components of the sensed wrench had an average error of $-$0.35 g with a standard deviation of 0.95 g, while the moment components had an average error of 0.11 mN·m with a standard deviation of 1.70 mN·m. The continuum

robot was also used to palpate a clinical prostate model. The generated surface-stiffness map matched the known pathological conditions of the model. These experimental results suggested a strong potential of using the continuum robots for surgical applications that require force feedback in confined spaces.

REFERENCES

[1] L. N. Verner and A. M. Okamura, "Sensor/actuator asymmetries in telemanipulators: Implications of partial force feedback," in *Proc. Symp. Haptic Interfaces Virtual Environ. Teleoperator Syst.*, Alexandria, VA, 2006, pp. 309–314.

[2] M. C. Cavusoglu, A. Sherman, and F. Tendick, "Design of bilateral teleoperation controllers for haptic exploration and telemanipulation of soft environments," *IEEE Trans. Robot. Autom.*, vol. 18, no. 4, pp. 641–647, Aug. 2002.

[3] C. R. Wagner, N. Stylopoulos, and R. D. Howe, "The role of force feedback in surgery: Analysis of blunt dissection," in *Proc. Symp. Haptic Interfaces Virtual Environ. Teleoperator Syst.*, Orlando, FL, 2002, pp. 68–74.

[4] K. Ikuta, S. Daifu, T. Hasegawa, and H. Higashikawa, "Hyper-finger for remote minimally invasive surgery in deep area," in *Proc. Int. Conf. Med. Image Comput. Comput.-Assist. Interv.*, Tokyo, Japan, 2002, pp. 173–181.

[5] M. Tavakoli, R. V. Patel, and M. Moallem, "A force reflective master-slave system for minimally invasive surgery," in *Proc. Int. Conf. Intell. Robots Syst.*, Las Vegas, NV, 2003, pp. 3077–3082.

[6] S. Shimachi, Y. Fujiwara, and Y. Hakozaki, "New sensing method of force acting on instrument for laparoscopic robot surgery," in *Proc. Comput. Assist. Radiol. Surg.*, Chicago, IL, 2004, pp. 775–780.

[7] U. Seibold, B. Kubler, and G. Hirzinger, "Prototype of instrument for minimally invasive surgery with 6-axis force sensing capability," in *Proc. IEEE Int. Conf. Robot. Autom.*, Barcelona, Spain, 2005, pp. 496–501.

[8] K. Tadano and K. Kawashima, "Development of 4-DoFs forceps with force sensing using pneumatic servo system," in *Proc. IEEE Int. Conf. Robot. Autom.*, Orlando, FL, 2006, pp. 2250–2255.

[9] M. Mitsuishi, N. Sugita, and P. Pitakwatchara, "Force feedback augmentation modes in the laparoscopic minimal invasive telesurgical system," *IEEE/ASME Trans. Mechatronics*, vol. 12, no. 4, pp. 447–454, Aug. 2007.

[10] D. T. Wallace, G. Stahler, A. Goldenberg, G. Reis, R. G. Younge, M. Clopp, D. Camarillo, and T. J. King St., "Method of sensing forces on a working instrument," U.S. Patent 0 197 9 39, Mountain View, CA: Hansen Medical, 2007.

[11] C. Sultan and R. Skelton, "A force and torque tensegrity sensor," *Sens. Actuators A: Phys.*, vol. 112, pp. 220–231, 2004.

[12] K. Xu and N. Simaan, "An investigation of the intrinsic force sensing capabilities of continuum robots," *IEEE Trans. Robot.*, vol. 24, no. 3, pp. 576–587, Jun. 2008.

[13] R. Ranganath, P. S. Nair, T. S. Mruthyunjaya, and A. Ghosal, "A force-torque sensor based on a stewart platform in a near-singular configuration," *J. Mech. Mach. Theory*, vol. 39, no. 9, Sep. 2004.

[14] M. Uchiyama, E. Bayo, and E. Palma-Villalon, "A systematic design procedure to minimize a performance index for robot force sensors," *J. Dyn. Syst., Meas., Control*, vol. 113, pp. 388–394, Sep. 1991.

[15] A. Bicchi, "A criterion for the optimal design of multi-axis force sensors," *Robot. Auton. Syst.*, vol. 10, pp. 269–286, 1992.

[16] M. M. Svinin and M. Uchiyama, "Optimal geometric structures of force/torque sensors," *Int. J. Robot. Res.*, vol. 14, no. 6, pp. 560–573, 1995.

[17] S. Hirose, *Biologically Inspired Robots, Snake-Like Locomotors and Manipulators*. Oxford, U.K.: Oxford Univ. Press, 1993.

[18] I. A. Gravagne and I. D. Walker, "Kinematic transformations for remotely-actuated planar continuum robots," in *Proc. IEEE Int. Conf. Robot. Autom.*, 2000, pp. 19–26.

[19] I. A. Gravagne and I. D. Walker, "Manipulability, force and compliance analysis for planar continuum manipulators," *IEEE Trans. Robot. Autom.*, vol. 18, no. 3, pp. 263–273, Jun. 2002.

[20] I. A. Gravagne and I. D. Walker, "On the kinematics of remotely-actuated continuum robots," in *Proc. IEEE Int. Conf. Robot. Autom.*, San Francisco, CA, 2000, pp. 2544–2550.

[21] N. Simaan, R. H. Taylor, and P. Flint, "A dexterous system for laryngeal surgery," in *Proc. IEEE Int. Conf. Robot. Autom.*, New Orleans, LA, 2004, pp. 351–357.

[22] B. A. Jones and I. D. Walker, "Practical kinematics for real-time implementation of continuum robots," *IEEE Trans. Robot. Autom.*, vol. 22, no. 6, pp. 1087–1099, Dec. 2006.

[23] G. H. Golub and C. F. Van Loan, *Matrix Computations*, 3rd ed. Baltimore, MD: The Johns Hopkins Univ. Press, 1996.

An Analytical Continuous-Curvature Path-Smoothing Algorithm

Kwangjin Yang and Salah Sukkarieh

***Abstract*—An efficient and analytical continuous-curvature path-smoothing algorithm, which fits an ordered sequence of waypoints generated by an obstacle-avoidance path planner, is proposed. The algorithm is based upon parametric cubic Bézier curves; thus, it is inherently closed-form in its expression, and the algorithm only requires the maximum curvature to be defined. The algorithm is, thus, computational efficient and easy to implement. Results show the effectiveness of the analytical algorithm in generating a continuous-curvature path, which satisfies an upper bound-curvature constraint, and that the path generated requires less control effort to track and minimizes control-input variability.**

***Index Terms*—Bézier curves, continuous-curvature path, path smoothing, upper bounded curvature constraint.**

I. INTRODUCTION

Nonholonomic motion planning in an obstacle-strewed environment is a difficult problem because the planner must simultaneously consider collision avoidance and nonholonomic constraints. Typical approaches involve generating a piecewise linear obstacle-free path using techniques such as A*, Voronoi diagrams, and probabilistic roadmaps [1]–[3] and then applying a secondary-smoothing algorithm over this linear path in order to generate a continuous path for the vehicle to follow.

The construction of smooth paths has been actively investigated by the mobile robot community because nonsmooth motions can cause slippage and overactuation [4]. Several methods have been applied, the most popular being Dubins curves [5]–[7]. This algorithm computes the shortest path between two postures in the plane via the concatenation of line segments and arcs of circles, taking into account the vehicles maximum rate of change of turn [8]. The Dubins method has been extended to other more-complex vehicle models but is still limited to line segments and arcs of circles. Discontinuities still arise at the junction of the line and arc in a Dubins curve, and these cause tracking errors. To overcome this problem, two categories of curves are used to generate a continuous-curvature path [9]. The first categories are those where the curvature is parameterized by the curve's arc length, such as Clothoids [9], [10]. Clothoid pairs provide smooth transitions with

Manuscript received October 27, 2009; revised February 3, 2010; accepted February 3, 2010. Date of publication March 11, 2010; date of current version June 9, 2010. This paper was recommended for publication by Associate Editor F. Lamiraux and Editor G. Oriolo upon evaluation of the reviewers' comments. This work was supported in part by the Australian Research Council (ARC) Centre of Excellence Program, funded by the ARC and the New South Wales State Government. This paper was presented in part at the IEEE/RSJ International Conference on Intelligent Robots and Systems, Nice, France, September 22–26, 2008.

The authors are with the Australian Centre for Field Robotics, The University of Sydney, Sydney, N.S.W. 2006, Australia (e-mail: k.yang@acfr.usyd.edu.au; salah@acfr.usyd.edu.au).

Color versions of one or more of the figures in this paper are available online at http://ieeexplore.ieee.org.

Digital Object Identifier 10.1109/TRO.2010.2042990